Distributed Hierarchical Control With Separation of Concerns for Parallel-Connected UPSs

Henrique Jank, William A. Venturini, Mário L. S. Martins, *Member, IEEE*, Humberto Pinheiro, *Member, IEEE*, and Fábio E. Bisogno, *Member, IEEE*

***Abstract*—This article presents a distributed hierarchical control structure for parallel uninterruptible power supplies. A dynamic approach with separation of concerns is proposed for the secondary control, where a so-called grid forming inverter is responsible for restoring the amplitude and frequency of the output voltage, while the remaining inverters, called grid supporting, are responsible for enhancing long-term power sharing. This strategy aims to minimize the tradeoff between voltage regulation and power sharing through secondary control, which uses a low bandwidth communication link. For the primary controller, resistive droop control with virtual resistance is employed to accomplish short-term power sharing. Simple design guidelines for the secondary controllers based on simplified models developed in the article are provided. Extensive experimental results obtained from two 500-VA prototypes demonstrated the good performance of the proposed strategy. The amplitude and power sharing errors remained below 1% and 2%, respectively, for the entire load range evaluated.**

***Index Terms*—Droop control, hierarchical control, parallelism of uninterruptible power supplies (UPSs), secondary control, separation of concerns.**

I. Introduction

In RECENT years, services such as transportation, telecommunications, e-commerce, entertainment, and banking are integrated and depend on large data centers. This scenario has intensified the demand for highly reliable and redundant power supplies. An alternative to obtain these features is the parallel connection of uninterruptible power supplies (UPSs). The parallelism of UPSs is a problem related to the parallel operation of inverters, whose challenge is to keep the voltages synchronized, with the same amplitude, frequency, and phase, in order to properly share the load [1].

Recently, hierarchical control structures that integrate some sort of communication to the well-known droop control, forming a multiloop structure, have been employed in order to improve the performance of paralleled inverters. These structures are mainly devoted to reduce the deviations of the voltage amplitude and frequency inherent to droop control. The hierarchy of this control consists basically on three levels, described as follows [2]. Level zero (0) comprises the inner control loops of the inverter, which are responsible for regulating the output voltage and limiting the current while maintaining the system stable. Level one (1), also called primary control, is responsible for stabilizing the parallelism and for establishing the power sharing. The droop control is employed to enhance system redundancy and enable plug-and-play functionality [3]. This level also includes a virtual impedance control loop that emulates a physical output impedance. Although its robustness and effectiveness in promoting the load sharing and system stabilization, the droop control suffers from inherent steady-state voltage amplitude and frequency regulation errors. These errors lead to the level two (2) on the hierarchy, named secondary control. This level is responsible for restoring the frequency and amplitude to their nominal values. Level two (2) often includes other control loops, such as a reactive power sharing [4]–[6] and synchronization loops [2]. As the outermost control loop, it permits the use of low bandwidth communication systems.

Secondary control strategies can be categorized as centralized, decentralized, or distributed [7]. Centralized approaches [8]–[14] are based on a communication system that connects all inverters to a central controller. The secondary control signals are calculated by this controller and transmitted to all inverters in order to restore the system voltage amplitude and frequency. However, any failure whether in the communication system or the central controller affects the overall stability and performance of the system.

In decentralized approaches [15]–[23], no communication is used for the secondary control. Each inverter restores its voltage amplitude and frequency separately and locally. However, a global communication system is still required for coordination of the inverter units during black start, plug-and-play processes, real-time monitoring, or other functionalities [7]. Due to the absence of communication, decentralized strategies tend to suffer from voltage and frequency deviations and poor power sharing [24].

Distributed secondary control [3]–[6], [25]–[29] is a communication-based approach that avoids the use of a single centralized controller. The primary and secondary controllers are implemented locally in each unit, where the secondary control

Manuscript received February 25, 2021; revised May 25, 2021; accepted July 15, 2021. Date of publication July 26, 2021; date of current version September 16, 2021. This work was financially supported in part by the Coordination for the Improvement of Higher Education Personnel – Brazil (CAPES/PROEX) – Finance Code 001, in part by the National Institute of Science and Technology in Distributed Generation (INCT-GD) – under grants CNPq 465640/2014-1, CAPES 23038.000776/2017-54 and FAPERGS 17/2551-0000517-1, and in part by the National Council for Scientific and Technological (CNPq) by financial support (proc. 423405/2018-7 and 308776/2018-6). Recommended for publication by Associate Editor M. Ordonez. *(Corresponding author: Henrique Jank.)*

The authors are with the Federal University of Santa Maria, Santa Maria 97105-900, Brazil (e-mail: hiquejank@gmail.com; williamventurini@gmail.com; mariolsm@gmail.com; humberto.ctlab.ufsm.br@gmail.com; fbisogno@gmail.com).

Digital Object Identifier 10.1109/TPEL.2021.3100016

should collect the required data from other units and produce an appropriate control signal for the primary level. In distributed control, the inverter units work together to cooperatively control the system and fulfill a set of objectives.

However, there is a challenge associated with distributed secondary control in relation to voltage stability and power sharing: The power sharing performance of P/E for resistive droop (or Q/E for inductive droop) is generally unsatisfactory [7]. This is because, unlike the frequency, the voltage amplitude is a local variable and is in a direct conflict with the active power [3], [5], [7]. This challenge is addressed in [3]–[6], [28]–[30].

A consensus-based distributed-averaging proportional-integral (DAPI) controller is proposed in [3] for improving voltage and frequency regulation in islanded microgrids. The frequency controller is able to regulate the microgrid frequency to its nominal value while maintaining good active power sharing among the distributed units. The voltage controller provides a tunable compromise between voltage amplitude regulation and reactive power sharing.

Distributed averaging secondary control techniques are proposed in [4] and [5] for restoring the voltage amplitude and frequency while improving reactive power sharing. However, there are two control loops with conflicting goals acting on the same control variable, i.e., the amplitude restoration and the reactive power sharing control signals are both used to adjust the voltage amplitude reference. This may lead the system to instability if the control signals are not limited, as both these controllers have integral signals and are parallel to each other. On the other hand, limiting the control signal of one of these controllers will lead to regulation errors for the respective control loop. Additionally, such approach presents difficulties when outages of inverter units occur [31].

Containment consensus-based distributed coordination controllers are employed in [6] and [30] for achieving accurate reactive power sharing while maintaining the voltage amplitudes of a microgrid bounded within a reasonable and predefined range. A distributed average integral secondary control (DAISC) for UPS-based microgrids is proposed in [28]. The inverter units share the integral output signal of the secondary controller in order to restore the voltage and frequency of the microgrid. However, power sharing objectives are coped by the primary controller alone, which is not accurate, especially when considering output impedance mismatches [3], [30].

A distributed voltage control based on the average consensus algorithm is proposed in [29]. The method combines the idea of secondary integral voltage control and regulator synchronization problem. It allows for an adjustable tradeoff between voltage regulation and power sharing. In general, the existing distributed hierarchical controllers can provide either: 1) Precise voltage regulation; b) precise power sharing; c) or an adjustable compromise between these objectives; according to the desired performance objectives [3], [29], [32].

This article proposes a distributed hierarchical control strategy that aims to minimize the tradeoff between voltage regulation and power sharing. This is achieved through the use of the separation of concerns concept, where a grid forming inverter (GFI) is responsible exclusively for voltage and frequency

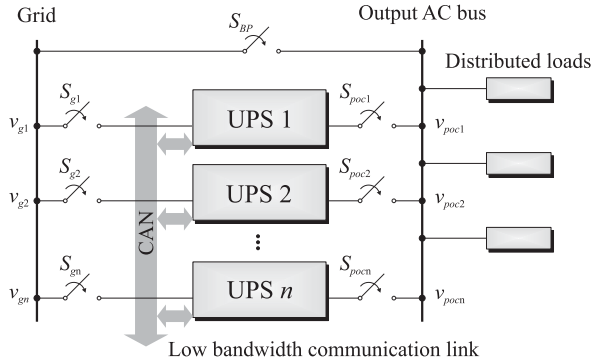

Fig. 1. System with n parallel-connected UPSs.

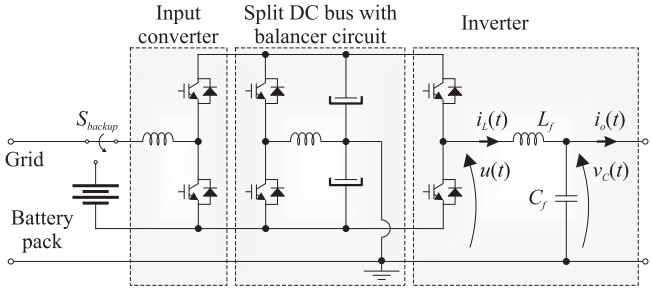

Fig. 2. Electrical diagram of the double-conversion UPSs.

restoration ($E\omega$ control), while the other parallel units, called grid supporting inverters (GSIs), are responsible for ensuring power sharing (PQ control).

The secondary control loops are implemented in every UPS, allowing each inverter to operate as either GFI or GSI. Thus, the system is able to remain operational in case of coordinator failure. Furthermore, the proposed method can rely to the droop mechanism even with overall communication system failure. Guidelines for designing the secondary control based on simplified models are provided. Experimental results from two inverter prototypes with a real controller area network (CAN)-based communication link are analyzed regarding voltage regulation, power sharing, plug-and-play capabilities, and performance under loss of communication. The main merits of the proposed method in comparison with the state of art are presented in Table I.

II. System Description

A simplified diagram of the investigated system is shown in Fig. 1. The system consists of n double-conversion UPSs operating in parallel, feeding a set of distributed loads through an ac bus. The UPSs communicate with each other through a low bandwidth CAN-based communication link. The UPS topology adopted is a transformerless single-phase double-conversion structure, as shown in the electrical diagram of Fig. 2.

Each UPS comprises an input converter, which acts as rectifier (in normal mode) or battery discharger (in backup mode); a split dc bus with an auxiliary circuit for balancing the dc bus voltages; and a half-bridge inverter with *LC* filter. The neutral terminal is common between input, dc bus midpoint, and output. Sinusoidal pulsewidth modulation (SPWM) is used as modulation scheme.

TABLE I
QUALITATIVE COMPARISON OF THE PROPOSED METHOD WITH THE STATE-OF-ART

	Centralized Control	Decentralized Control	Distributed Control					
			Proposed	[3]	[4], [5]	[6], [30]	[28]	[29]
Robust to single-point failure	No	Yes	Yes	Yes	Yes	Yes	Yes	Yes
Plug and play capability	Low	High	High	High	High	High	High	High
Communication robustness	Low	-	High	High	High	High	High	High
Voltage and frequency regulation	Good	Good	Very good	Good	Good	Good	Very good	Good
Power sharing performance	Good	Reasonable	Very good	Good	Good	Good	Good	Good
Tradeoff between voltage regulation and power sharing	Low	Low	Low	Adjustable	High	Adjustable	Low	Adjustable

While this study investigates the aforementioned UPS structure, the concepts can be applied to other topologies as well as its three-phase counterpart, with minor modifications [33].

In normal operating mode, the UPSs feed the loads from the grid. When a fault occurs or when the grid voltage is outside preset limits, the UPSs operate in backup mode, in which the grid is disconnected by the switches $S_{g1,g2,\ldots gn}$ and the UPSs feed the loads from a battery pack. The system can also operate in bypass mode during maintenance events or in case of failure of some equipment. During this mode, the UPSs are disconnected from the grid by $S_{g1,g2,\ldots gn}$ and from the output ac bus by $S_{\text{poc1,poc2,}\ldots\text{poc}n}$. In this mode, the loads are fed directly by the grid via the bypass switch (S_{BP}). During normal and backup modes, the UPSs must share the load power demand by adjusting their voltage references in accordance to the active and reactive powers delivered by each of the n inverters.

III. CONTROL SYSTEM

This section describes the proposed distributed hierarchical control with separation of concerns (DHCSC). First, the inner control loops and primary control are described. The main contributions of the article are detailed at the secondary control level, which comprises a strategy with separation of concerns. Finally, an alternative is presented to improve voltage regulation in case of total communication failure, based on the robust droop controller (RDC) proposed in [15].

A. Level 0: Inner Loops

Current and voltage control loops are implemented at this level, as shown in the block diagram of Fig. 3. An inner current feedback control loop with a proportional controller (k_{ci}) is used for precompensating the plant, in addition to providing current limiting capability in case of overload or short-circuit. A full-state feedback control law is used for the outer voltage feedback control loop. A set of resonant controllers tuned at the fundamental frequency (Res_1) and harmonics of order 3, 5, and 7 ($\text{Res}_{3,5,7}$) are included to ensure sinusoidal reference

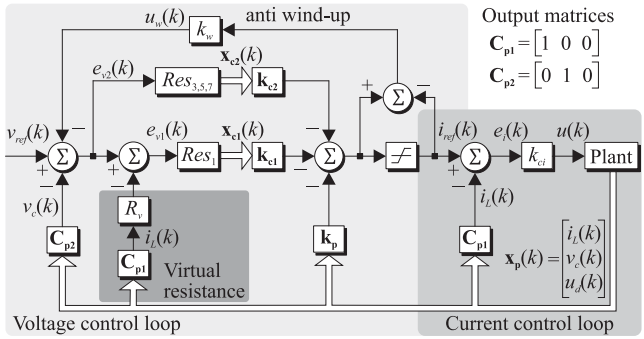

Fig. 3. Diagram of blocks for voltage and current control loops (Level 0).

tracking and rejection of periodic disturbances. The states of the plant, $\mathbf{x_p}(k)$, and the states of resonant controllers, $\mathbf{x_{c1}}(k)$ and $\mathbf{x_{c2}}(k)$, are compensated by the gain vectors $\mathbf{k_p}$, $\mathbf{k_{c1}}$, and $\mathbf{k_{c2}}$, respectively, to generate the current reference. $\mathbf{C_{p1}}$ and $\mathbf{C_{p2}}$ are the output matrices for the states $i_L(k)$ and $v_c(k)$, respectively. The gain vectors $\mathbf{k_p}$, $\mathbf{k_{c1}}$, and $\mathbf{k_{c2}}$ are designed by means of a linear quadratic regulator (LQR). An anti wind-up loop with a proportional gain (k_w) is included to adjust the voltage reference when the system operates in current limiting mode.

A virtual resistance (R_v) is employed to ensure a resistive output impedance for the inverters. It is worth noting from Fig. 3 that the virtual resistance is applied only to the fundamental resonant controller, preventing the harmonic resonant controllers to be affected by it. This approach should improve the output voltage harmonic distortions.

B. Level 1: Primary Control

This level is responsible for generating the references of amplitude (E_d) and frequency (ω_d) for the inverter inner control loops. Droop control is used to establish power sharing while avoiding the use of critical communication among the inverters. Resistive droop control was chosen here because it fits low-voltage applications such as parallel-connected UPSs, which present purely resistive line impedances [2], [34]. In addition, it

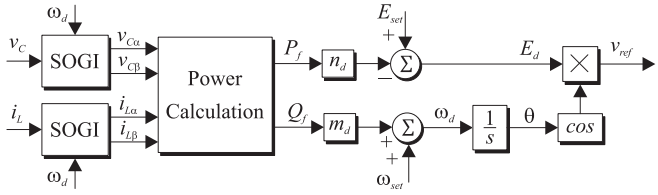

Fig. 4. Primary control: Resistive droop control.

provides proper damping [16], causes less harmonic distortion in the output voltage [35] and aids to reduce the circulating currents [36]. The block diagram of the resistive droop control is shown in Fig. 4, and the references for amplitude and frequency are given by

$$E_d = E_{set} - n_d P_f, \quad \omega_d = \omega_{set} + m_d Q_f \tag{1}$$

where P_f and Q_f are the active and reactive power, respectively; and E_{set} and ω_{set} are, respectively, the setpoints of amplitude and frequency, established, in this case, by the secondary control.

The coefficients n_d and m_d define the slope of the voltage drop and frequency increase curves, respectively. These coefficients are designed according to acceptable amplitude and frequency deviations for a certain—usually nominal—active and reactive power, respectively, as

$$n_d = \frac{\Delta E}{\Delta P}, \quad m_d = \frac{\Delta \omega}{\Delta Q}. \tag{2}$$

The instantaneous powers are obtained from the voltage and current on the $\alpha\beta$-frame as

$$p = \frac{v_{c\alpha} i_{L\alpha} + v_{c\beta} i_{L\beta}}{2}, \quad q = \frac{v_{c\beta} i_{L\alpha} - v_{c\alpha} i_{L\beta}}{2} \tag{3}$$

which, in turn, are obtained by means of a second-order generalized integrator (SOGI) [37].

The instantaneous power values are filtered by first-order low-pass filters with cutoff frequencies ω_P and ω_Q, thus

$$P_f = \frac{\omega_P}{s + \omega_P} p, \quad Q_f = \frac{\omega_Q}{s + \omega_Q} q. \tag{4}$$

C. Level 2: Secondary Control

The secondary control is responsible for adjusting the amplitude and frequency setpoints for the primary control, compensating the inherent deviations of droop control and improving power sharing. At this level, a low bandwidth communication link is used to transmit the values of amplitude, frequency, and active and reactive power among all UPSs. The number of parallel-connected inverters is known due to the communication link, allowing computation of the average of the transmitted quantities used by the secondary control.

The secondary control is comprised of a synchronous reference frame phase-locked loop (SRF-PLL) [37], which maintains the UPSs output voltages synchronized with the grid voltage, allowing a proper transfer to bypass mode. The application of SRF-PLL to single-phase inverters is proposed in [38] by using SOGI.

Besides the PLL, secondary control comprises four other control loops: Amplitude and frequency restoration; and active and reactive power sharing. The amplitude restoration loop and the active power sharing loop act to control the amplitude setpoint. Similarly, the PLL, the frequency restoration loop and the reactive power sharing loop act to control of the frequency setpoint. That is, there are different control loops with distinct goals acting on the same variables. Therefore, to prevent these actions from interfering with each other, an approach with separation of concerns is proposed.

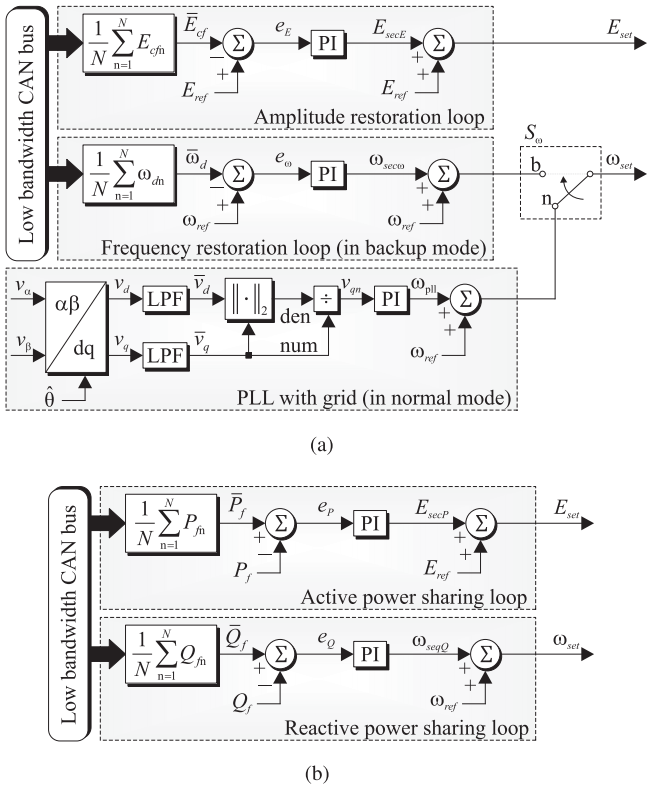

Fig. 5. Distributed secondary control loops. (a) GFI. (b) GSI.

The proposed control strategy is shown in the block diagram of Fig. 5, where Fig. 5(a) shows the control loops for the GFI, while Fig. 5(b) presents those for the GSI. It is worth mentioning that all five secondary control loops are implemented in every UPS, allowing each inverter to operate as either GFI or GSI. This way, in the case of a GFI failure, the system is able to remain operational. The identification (ID) of each inverter is shared on the communication bus and the grid forming function is assigned to the available inverter with the lowest ID (highest priority in CAN protocol).

1) Amplitude Restoration: The amplitude restoration loop compensates the voltage deviation caused by droop control and virtual resistance in both normal and backup modes. Initially, the amplitude of the output voltage is calculated by each inverter from the $\alpha\beta$ components, and then filtered by means of a first-order low-pass filter with cutoff frequency ω_{lpfE}, in order to attenuate oscillations, according to

$$E_{cf} = \frac{\omega_{\text{lpfE}}}{s + \omega_{\text{lpfE}}} \sqrt{{v_{c\alpha}}^2 + {v_{c\beta}}^2}. \tag{5}$$

The output voltage amplitude E_{cf} is transmitted through the CAN bus, allowing the calculation of the average ($\bar{E}_{cf}$) of all voltage amplitudes, which is then compared to the nominal value and the error generated is compensated by a PI controller. The respective control signal is

$$E_{\text{secE}} = \frac{k_{pE}s + k_{iE}}{s}\left(E_{\text{ref}} - \bar{E}_{cf}\right) \tag{6}$$

where k_{pE} and k_{iE} are the proportional and integral gains, respectively.

With this strategy, the GFI is able to remove the voltage deviations caused by the primary controller in each UPS, maintaining the average voltage amplitude regulated at the reference value with no steady-state error.

2) Frequency Restoration: The frequency restoration loop is used by the GFI in backup mode, since in normal mode the UPSs must be synchronized with the grid. This control loop acts to restore the average frequency of all inverters, compensating the deviations caused by droop control.

The frequency value obtained in the primary control by (1) is transmitted through the CAN bus, allowing the calculation of average frequency, which is then compared to its nominal value in order to generate a control signal given by

$$\omega_{\text{sec}\omega} = \frac{k_{p\omega}s + k_{i\omega}}{s}(\omega_{ref} - \bar{\omega}_d) \tag{7}$$

where $k_{p\omega}$ and $k_{p\omega}$ are the proportional and integral gains, respectively.

Thus, in steady state, the GFI is able to keep the frequency regulated at its nominal value with no steady-state error.

3) Active Power Sharing: The GSIs act with an active power sharing loop in order to maintain the active power of the UPSs equalized. The active power sharing loop uses the average value of active power from all UPSs as its reference, compensating the error by means of a PI controller and generating a control signal according to

$$E_{\text{sec}P} = \frac{k_{pP}s + k_{iP}}{s}\left(\bar{P}_f - P_{f\text{n}}\right) \tag{8}$$

where k_{pP} and k_{pP} are the proportional and integral gains, respectively.

Since the active power reference obtained is common to all inverters, accurate power sharing is obtained.

4) Reactive Power Sharing: The average reactive power is used as a reference value for the reactive power sharing control loop. The control signal is given by

$$\omega_{\text{sec}\,Q} = \frac{k_{pQ}s + k_{iQ}}{s}\left(\bar{Q}_f - Q_{f\text{n}}\right) \tag{9}$$

where k_{pQ} and k_{pQ} are the proportional and integral gains.

The PI controller ensures that reactive power is maintained at the reference value, assuring that the GSIs are synchronized with the GFI. Reactive power sharing is obtained naturally for the GFI, since the reactive power of each of the GSIs is regulated at the reference value (average power).

D. Local Amplitude Restoration Loop

The system is able to remain in operation through the primary control even with a communication link outage. In order to improve the voltage regulation of conventional droop control in the absence of communication, an approach based on the RDC proposed in [15] is used, where each inverter utilizes a local amplitude restoration control loop. The block diagram of this control is shown in Fig. 6. The frequency droop control shown in Fig. 4 is maintained, while for amplitude, the local restoration loop is implemented.

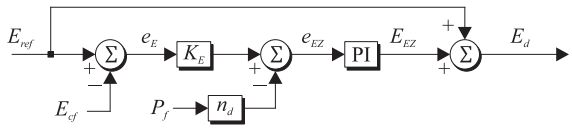

Fig. 6. Robust droop controller with local amplitude restoration loop.

TABLE II
SYSTEM PARAMETERS

Parameter	Symbol	Value
Output voltage (RMS)	V_o, f_g	127 V, 60 Hz
Nominal apparent power (each inverter)	S_{nom}	500 VA
DC bus total voltage	V_{DC}	450 V
Switching/sampling frequency	f_{sw}, f_s	15 kHz, 15 kHz
Output filter inductor and capacitor	L_f, C_f	3 mH, 10 μF
Nominal load resistance (each inverter)	R_{nom}	32.2 Ω

In this case, the voltage amplitude is compared to the reference value, generating an error signal e_E. From this error and a proportional portion of the active power (from conventional droop control), a modified error signal is generated, as in

$$e_{EZ} = K_E e_E - n_d P_f. \tag{10}$$

The modified error is compensated by a PI controller, generating the amplitude reference for the inner loops, as in

$$E_d = \frac{k_{pZ}e_{EZ}s + k_{iZ}e_{EZ}}{s} + E_{\text{ref}}. \tag{11}$$

Since the voltage amplitude and its reference are dc signals, if the system is stable, the input of the PI controller at steady-state operation is null, that is, $e_{EZ} = 0$ and, from (11)

$$K_E e_E = n_d P_f. \tag{12}$$

From (12), the value of K_E can be adjusted according to the maximum allowed amplitude deviation for a certain active power value. By choosing $K_E = 1$, the amplitude deviation introduced by the virtual resistance is eliminated at steady-state operation, remaining only the deviation introduced by the action of the droop control. The proportional (k_{pZ}) and integral (k_{iZ}) gains of the PI controller can be designed to adjust the dynamic response of the system.

IV. MODELING AND CONTROL SYSTEM DESIGN

This section presents the system modeling and a design example for two UPS inverter prototypes implemented in the laboratory, whose main parameters are presented in Table II.

A. Level 0: Inner Loops

From the inverter circuit of Fig. 2, one has

$$\dot{\mathbf{x}}(t) = \mathbf{A}\mathbf{x}(t) + \mathbf{B}u(t) + \mathbf{B_i}i_o(t)$$
$$\mathbf{x}(t) = \begin{bmatrix} i_L(t) \\ v_c(t) \end{bmatrix}, \quad \mathbf{A} = \begin{bmatrix} 0 & -\frac{1}{L_f} \\ \frac{1}{C_f} & 0 \end{bmatrix}$$
$$\mathbf{B} = \begin{bmatrix} \frac{1}{L_f} \\ 0 \end{bmatrix}, \quad \mathbf{B_i} = \begin{bmatrix} 0 \\ -\frac{1}{C_f} \end{bmatrix}. \tag{13}$$

The discrete-time model

$$\mathbf{x_p}(k+1) = \mathbf{G_2}\mathbf{x_p}(k) + \mathbf{H_2}u(k) + \mathbf{H_{i2}}i_o(k)$$
$$\mathbf{G_2} = \begin{bmatrix} \mathbf{G_1} & \mathbf{H_1} \\ \mathbf{0} & 0 \end{bmatrix}, \quad \mathbf{H_2} = \begin{bmatrix} \mathbf{0} \\ 1 \end{bmatrix}$$
$$\mathbf{H_{i2}} = \begin{bmatrix} \mathbf{H_{i1}} \\ 0 \end{bmatrix}, \quad \mathbf{x_p}(k) = \begin{bmatrix} \mathbf{x}(k) \\ u_d(k) \end{bmatrix} \tag{14}$$

is obtained by means of the zero-order hold (ZOH) method, being $\mathbf{G_1}$ the dynamic matrix, $\mathbf{H_1}$ the control input matrix, and $\mathbf{H_{i1}}$ the disturbance input matrix, obtained from the discretization of (13). The state u_d represents the delay from the implementation of the control law.

Note from Fig. 3 that

$$i_L(k) = \mathbf{C_{p1}}\mathbf{x_p}(k), \quad \mathbf{C_{p1}} = \begin{bmatrix} 1 & 0 & 0 \end{bmatrix}$$
$$v_c(k) = \mathbf{C_{p2}}\mathbf{x_p}(k), \quad \mathbf{C_{p2}} = \begin{bmatrix} 0 & 1 & 0 \end{bmatrix}. \tag{15}$$

The expression $u(k)$ is given by

$$u(k) = k_{ci}\left(i_{ref}(k) - \mathbf{C_{p1}}\mathbf{x_p}(k)\right). \tag{16}$$

The current reference—assuming operation in the linear region (with no current limitation)—is

$$i_{\text{ref}}(k) = -\begin{bmatrix} \mathbf{k_p} & \mathbf{k_{c1}} & \mathbf{k_{c2}} \end{bmatrix}\begin{bmatrix} \mathbf{x_p}(k) \\ \mathbf{x_{c1}}(k) \\ \mathbf{x_{c2}}(k) \end{bmatrix}. \tag{17}$$

By replacing (16) and (15) in (14) one has

$$\mathbf{x_p}(k+1) = \mathbf{G_3}\mathbf{x_p}(k) + \mathbf{H_3}i_{\text{ref}}(k) + \mathbf{H_{i2}}i_o(k)$$
$$\mathbf{G_3} = \mathbf{G_2} - k_{ci}\mathbf{H_2}\mathbf{C_{p1}}, \quad \mathbf{H_3} = k_{ci}\mathbf{H_2}. \tag{18}$$

The resonant controllers Res_1 and $\text{Res}_{3,5,7}$ can be described, respectively, in the state space form as

$$\mathbf{x_{c1}}(k+1) = \mathbf{G_{c1}}\mathbf{x_{c1}}(k) + \mathbf{H_{c1}}e_{v1}(k)$$
$$\mathbf{x_{c2}}(k+1) = \mathbf{G_{c2}}\mathbf{x_{c2}}(k) + \mathbf{H_{c2}}e_{v2}(k)$$
$$\mathbf{G_{c1}} = \begin{bmatrix} 0 & 1 \\ g(\omega_i) & h(\omega_i) \end{bmatrix}, \quad \mathbf{H_{c1}} = \begin{bmatrix} 0 \\ 1 \end{bmatrix}$$
$$\mathbf{G_{c2}} = \text{diag}\left(\begin{bmatrix} 0 & 1 \\ g(\omega_i) & h(\omega_i) \end{bmatrix} \cdots \begin{bmatrix} 0 & 1 \\ g(\omega_i) & h(\omega_i) \end{bmatrix}\right)$$

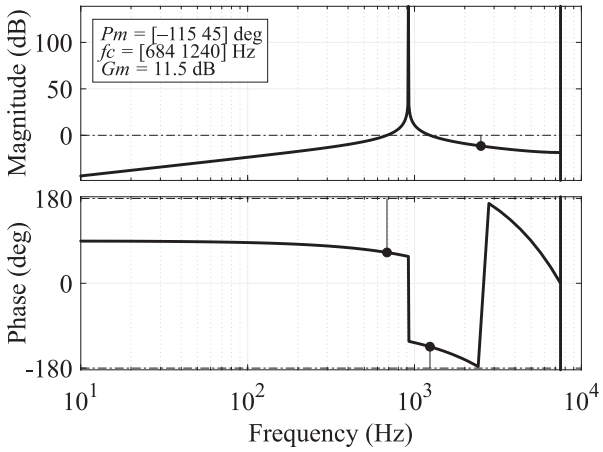

Fig. 7. Open loop Bode plot of the compensated current plant.

$$\mathbf{H_{c2}} = \begin{bmatrix} 0 & 1 & \dots & 0 & 1 \end{bmatrix}^T$$
$$g(\omega_i) = -\exp(-2T_s\xi\omega_i)$$
$$h(\omega_i) = 2\cos(T_s\omega_i)\exp(-T_s\xi\omega_i) \tag{19}$$

where ξ is the damping factor and ω_i is the frequency of the resonant controller of ith order.

The voltage errors—once again, assuming operation in the linear region—are given by

$$e_{v1}(k) = v_{ref}(k) - R_v\mathbf{C_{p1}}\mathbf{x_p}(k) - \mathbf{C_{p2}}\mathbf{x_p}(k)$$
$$e_{v2}(k) = v_{\text{ref}}(k) - \mathbf{C_{p2}}\mathbf{x_p}(k). \tag{20}$$

From (18), (19), and (20), one can write the expanded system as

$$\mathbf{x_s}(k+1) = \mathbf{G_4}\mathbf{x_s}(k) + \mathbf{H_4}i_{\text{ref}}(k) + \mathbf{H_v}v_{\text{ref}}(k) + \mathbf{H_i}i_o(k)$$
$$\mathbf{G_4} = \begin{bmatrix} \mathbf{G_3} & \mathbf{0} & \mathbf{0} \\ -\mathbf{H_{c1}}(R_v\mathbf{C_{p1}} + \mathbf{C_{p2}}) & \mathbf{G_{c1}} & \mathbf{0} \\ -\mathbf{H_{c2}}\mathbf{C_{p2}} & \mathbf{0} & \mathbf{G_{c2}} \end{bmatrix}$$
$$\mathbf{H_4} = \begin{bmatrix} \mathbf{H_3} \\ \mathbf{0} \\ \mathbf{0} \end{bmatrix}, \quad \mathbf{H_v} = \begin{bmatrix} \mathbf{0} \\ \mathbf{H_{c1}} \\ \mathbf{H_{c2}} \end{bmatrix}, \quad \mathbf{H_i} = \begin{bmatrix} \mathbf{H_{i2}} \\ \mathbf{0} \\ \mathbf{0} \end{bmatrix}. \tag{21}$$

Finally, the close loop system is described by

$$\mathbf{x_s}(k+1) = \mathbf{G_s}\mathbf{x_s}(k) + \mathbf{H_v}v_{ref}(k) + \mathbf{H_i}i_o(k)$$
$$\mathbf{G_s} = \mathbf{G_4} - \mathbf{H_4}\begin{bmatrix} \mathbf{k_p} & \mathbf{k_{c1}} & \mathbf{k_{c2}} \end{bmatrix}. \tag{22}$$

The current control loop proportional gain was designed based on the bode plot of the inductor current i_L in relation to the current error $e_i(k)$. The gain value is adjusted to achieve a gain margin above 10 dB and a phase margin above 45 deg. The obtained gain value was $k_{ci} = 10.476$, and the corresponding bode plot is shown in Fig. 7. As for the virtual resistance, a value between 0.05 and 0.15 pu on the inverter base is considered to be a proper design [39]. Thus, a virtual resistance of 0.1 pu [40] was chosen here.

TABLE III
PRIMARY CONTROL PARAMETERS

Parameter	Symbol	Value
Droop coefficients	n_d, m_d	17×10^{-3}, 15×10^{-3}
Power filter cutoff frequencies	ω_P, ω_Q	6 Hz, 6 Hz
Virtual resistance	R_v	3.22Ω

Finally, the gain vectors k_p, k_{c1}, and k_{c2} were designed by means of an LQR due to its advantageous properties, such as large stability margins. The LQR solution is based on Riccati's equation [41] and the control gains can be easily obtained by means of the dlqr function in MATLAB, by using the matrices $\mathbf{G_4}$ and $\mathbf{H_4}$ from the state-space model as input arguments. The design of good LQR controllers depends fundamentally on the choice of the weighting matrices $\mathbf{Q}$ and $\mathbf{R}$, and generally requires some trial and error sessions until a good dynamic response is obtained. After several tests, a good dynamic response was obtained by using the matrices

$$\mathbf{Q} = \text{diag}\left(\begin{bmatrix} 5 & 1 & 1 & 16_{1\times 2} & 1.7_{1\times 2} & 1.2_{1\times 2} & 0.5_{1\times 2}\end{bmatrix}\right)$$
$$\mathbf{R} = 7.5 \times 10^8. \tag{23}$$

The obtained state feedback gains were

$$\mathbf{k_p} = \begin{bmatrix} 0.286882 \\ 0.012629 \\ 0.006929 \end{bmatrix}^T, \quad \mathbf{k_{c2}} = \begin{bmatrix} 0.000687 \\ -0.000724 \\ 0.000424 \\ -0.000431 \\ 0.000185 \\ -0.000179 \end{bmatrix}^T.$$
$$\mathbf{k_{c1}} = \begin{bmatrix} 0.005915 \\ -0.006046 \end{bmatrix}^T, \tag{24}$$

The damping factor used for the resonant controllers was $\xi = 5 \times 10^{-4}$.

B. Level 1: Primary Control

The dynamic performance of the droop control is associated with the dynamics of the filters used in the power quantities calculation [42]. Thus, the cutoff frequency must be sufficiently small, usually a decade below grid frequency, in order to decouple the dynamics of levels 0 and 1 [43].

The droop coefficients were defined based on the maximum allowable amplitude and frequency deviations from (2). Maximum deviations of 5% and 2% for the amplitude and frequency, respectively, were adopted [1]. For the maximum active and reactive power deviations (ΔP and ΔQ, respectively), the rated apparent power (S_{nom}) was considered. The main parameters of primary control, along with the virtual resistance, are summarized in Table III.

C. Level 2: Secondary Control

A complete modeling of the parallel-connected inverter system is extensive and complex, involving several coupled variables. Therefore, simplified models were obtained in order to propose a simple design procedure. In these models, the operation of a single inverter was considered and the contribution of the droop control was neglected. Additionally, the dynamics of the control loop of interest were isolated, while the dynamics of the other control loops were considered disturbances.

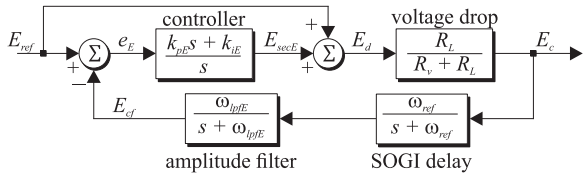

Fig. 8. Simplified model of the amplitude restoration loop.

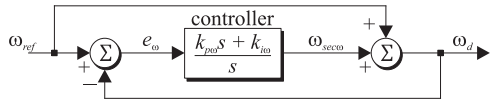

Fig. 9. Simplified model of the frequency restoration loop.

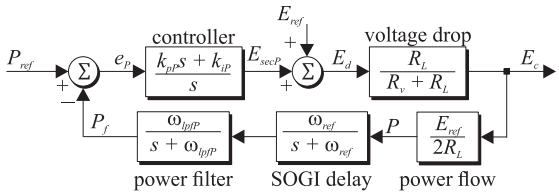

Fig. 10. Simplified model of the active power sharing loop.

1) Amplitude Restoration Loop: A simplified model that relates the amplitude of the output voltage to the amplitude reference is shown in Fig. 8. The model considers the controller, a voltage drop due to the load effect (for a resistive load R_L and the virtual resistance) and the delays introduced by the SOGI and the power filter.

2) Frequency Restoration Loop: A simplified model that relates the frequency of the output voltage to the reference frequency is shown in the block diagram of Fig. 9.

3) Active Power Sharing Loop: The active power sharing loop acts on the voltage amplitude of the GSIs in order to equalize the system's active powers. A model that relates the output voltage amplitude to the active power reference ($\bar{P}_f = P_{\text{ref}}$) is shown in Fig. 10. This model includes the controller, the voltage drop from virtual resistance and load effect, the power flow equation and SOGI, and power filter delays. The power flow equation in Fig. 10 is obtained from the power fed to a resistive load—which is $P = \frac{{E_c}^2}{2R_L}$—by assuming a small voltage deviation so that $E_c \approx E_{\text{ref}}$.

4) Reactive Power Sharing Loop: This control loop acts on the frequency of the output voltage of the GSIs in order to equalize the system's reactive powers. A model that relates the output voltage frequency to the reactive power reference ($\bar{Q}_f = Q_{ref}$) is shown in Fig. 11. This model includes the controller, an integrator (to obtain the phase angle δ), the power flow equation and SOGI and power filter delays. It is worth noting that the power flow equation in Fig. 11 is obtained from the reactive power fed to an ideal bus—which is $Q = -\frac{E_o E_c}{2R_v}\sin(\delta)$—by

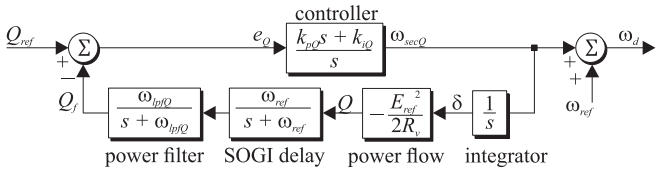

Fig. 11. Simplified model of the reactive power sharing loop.

TABLE IV
SECONDARY CONTROL GAINS

Control loop	Symbol	Value
Amplitude restoration	k_{pE}, k_{iE}	0.0122, 42.626
Frequency restoration	$k_{p\omega}$, $k_{i\omega}$	0.1, 3.125
Active power sharing	k_{pP}, k_{iP}	0.189, 7.56
Reactive power sharing	k_{pQ}, k_{iQ}	-4.22×10^{-3}, -2.11×10^{-4}

assuming a small voltage deviation so that $E_c \approx E_o \approx E_{\text{ref}}$ and a small phase angle so that $\sin(\delta) \approx \delta$; where E_o is the ideal bus voltage amplitude.

5) Secondary Control Design: The design of the distributed secondary control gain values was based on the frequency response analysis of the simplified models obtained in Section IV-C. The cutoff frequencies of the open-loop response of the secondary control must be small enough to ensure an adequate decoupling from the primary control (in this case, smaller than the cutoff frequency of the power filters). The design considered $R_L = R_{\text{nom}}$ and, for all control loops, a phase margin above 60 deg was desired.

Both the amplitude restoration and the active power sharing loops act on the output voltage amplitude. Cutoff frequencies of about 6 and 6 Hz are desired for these control loops, respectively.

For the frequency restoration control loop, a cutoff frequency of about 0.5 Hz is defined. There is a correlation between the frequency restoration and reactive power sharing control loops, as both act on the frequency of the inverter output voltages. Thus, the reactive power sharing control loop of the GSIs should provide a faster response than that provided by the frequency restoration control loop of the GFI. Therefore, a cutoff frequency around 3 Hz is defined.

The gain values of each secondary control loop are shown in Table IV and the bode plots in Fig. 12, with the respective values of phase margin and cutoff frequency. As the design was carried out for a nominal load condition, a stability analysis for load variations is presented in the Appendix.

V. EXPERIMENTAL RESULTS

In order to demonstrate the advantages and limitations of the proposed DHCSC, a set of laboratory tests was carried out. The analyses are divided into steady-state and transient results. Two UPS prototypes were built. The main parameters are presented in Table II. It should be noted that only the inverter stage for the UPS units was implemented and the dc buses were obtained from two dc power sources. The control system was implemented independently in each inverter in digital signal processors (model TMS320F28335). The CAN bus transmission

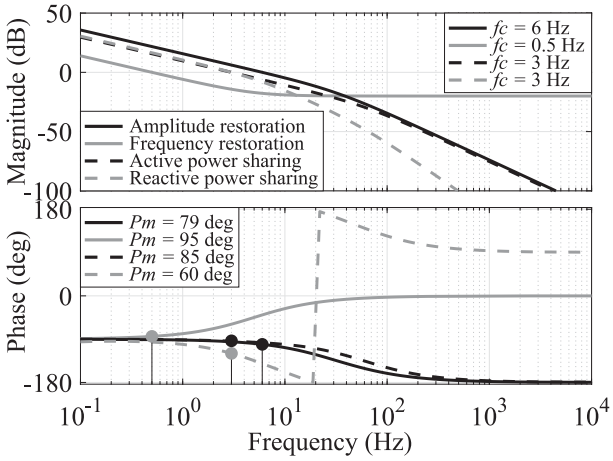

Fig. 12. Bode diagrams of the secondary control loops.

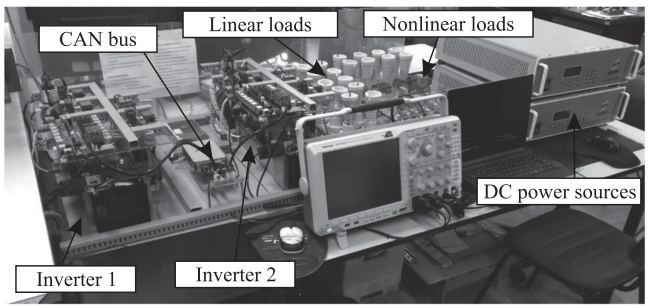

Fig. 13. Laboratory prototype with two parallel-connected inverters.

rate was 500 Hz. A photograph of the two paralleled inverters can be seen in Fig. 13.

The results for the slow dynamic variables, i.e., amplitudes, frequencies, and powers, are obtained via CAN from an NI-9862 interface module. Additionally, as no differences were observed in terms of performance for both operating modes, only results for the normal mode are presented. From here on, the variables with subscript 1 will be used to refer exclusively to the GFI.

A. Steady-State Results

The first test of steady-state operation was carried out at no load condition. A second test was performed considering operation with a nominal linear load, followed by a final test with nominal nonlinear loads in accordance with IEC 62 040-3 [44] specifications. The nonlinear load consisted of a diode bridge with a bulky capacitor and a resistive load at the dc side. The load voltage (v_{load}), the output currents (i_{o1} and i_{o2}), and the circulating current (i_c) are shown for no load condition in Fig. 14(a), for nominal linear load in Fig. 14(b) and for nominal nonlinear load in Fig. 14(c). In all three cases the load voltage was regulated at its nominal value and the output currents were symmetrical to each other, while the circulating current was mainly composed of high-frequency components, indicating good power sharing, and adequate parallel operation. Additionally, the output voltage THD obtained for operation with the nominal nonlinear load (the worst case scenario) was 3.45%, which complies with the 8% limit of the IEC 62 040-3 Standard.

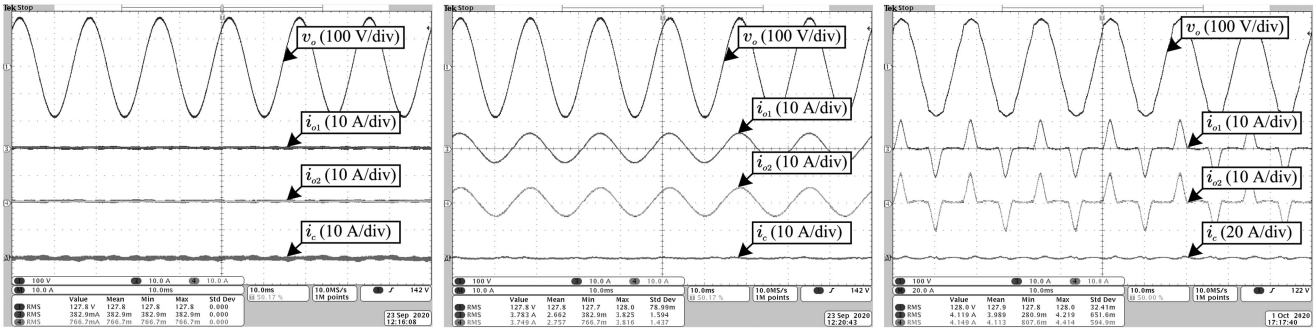

Fig. 14. Steady-state results. (a) Load voltage and output currents for no load operation. (b) Load voltage and output currents for nominal linear load. (c) Load voltage and output currents for nominal nonlinear load.

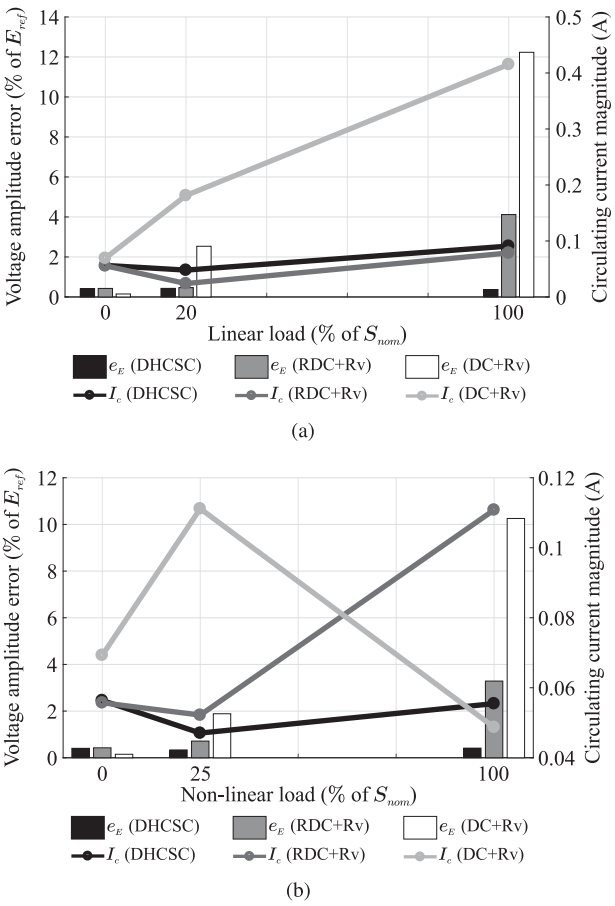

Fig. 15. Steady-state quantitative results. (a) Amplitude error and circulating currents at the fundamental frequency for linear load. (b) Amplitude error and circulating currents at the fundamental frequency for nonlinear load.

Fig. 15 shows some quantitative results analyzed at the fundamental frequency. The results for the proposed DHCSC were compared to the results obtained from the standard droop controller with virtual resistance (dc+Rv) and the robust droop controller with virtual resistance (RDC+Rv) described in Section III-D. Fig. 15(a) and (b) shows the amplitude error ($e_{E\%}$) and the circulating current amplitude (I_c) as a function of the linear and nonlinear load demand, respectively. It can be noted that the amplitude error for the proposed strategy remained below 1% for all load conditions, while the error at nominal load was about 4% and 11% for the RDC+Rv and dc+Rv, respectively.

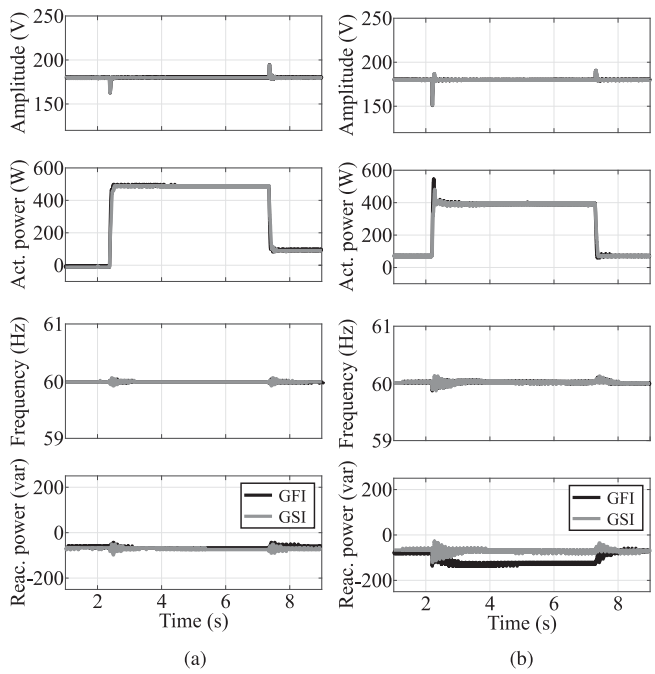

Fig. 16. Transient results. (a) Amplitudes, frequencies, active and reactive powers for linear load steps. (b) Amplitudes, frequencies, active and reactive powers for nonlinear load steps.

The proposed method also presented lower circulating currents, particularly at nominal load.

B. Transient Results

To test the system's transient response to linear load steps, the system was started with a linear load of 20% of nominal power. Then, a linear load consisting of 80% of nominal power was connected and removed after a few seconds.

Fig. 16(a) shows the amplitudes, frequencies, and active and reactive powers of the two inverters for this test. When the load was increased, there was a voltage drop due to droop control and virtual resistance, which was compensated by the amplitude restoration loop, reaching steady state after about 160 ms. The active power of the two inverters was properly shared even during the load transient. The frequencies and reactive powers only underwent small disturbances.

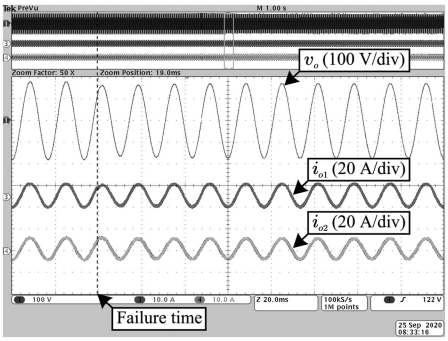

Fig. 17. Communication system outage result.

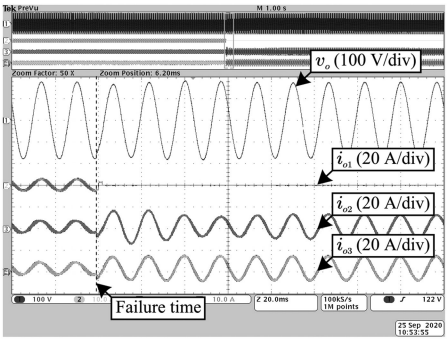

Fig. 18. GFI failure and redefinition.

Tests for nonlinear load steps were also performed, where the system initiated with a nonlinear load consisting of 25% of the nominal apparent power. A nonlinear load step consisting of 75% of the nominal apparent power was then applied and removed after a few seconds. The amplitudes, frequencies, and active and reactive powers of the two inverters for this test are shown in Fig. 16(b). The large voltage drop seen in the load increase step occurred because the capacitors of the dc side of the nonlinear load were completely discharged at the moment the loads were connected. It can be noted that accurate power sharing was achieved and the voltage reached its nominal value about 160 ms after applying the load step. There were small disturbances in the frequencies when the load steps were applied.

A test to assess system performance when the communication system fails is performed. The system starts operating normally, with linear load at rated power. Then, the communication cable of one of the inverters is removed and the system starts to operate with a local controller by means of the robust droop controller described in Section III-D. Fig. 17 shows the load voltage and the output currents for this test. A smooth transient response is perceived, and the system remains operating with a small steady-state voltage amplitude deviation, as expected.

Finally, a test emulating the failure and redefinition of the GFI is performed. As the prototype consists of only two inverters, the failure of the GFI would result in the operation of a single inverter. Thus, the test is carried out on a hardware-in-the-loop platform (Typhoon HIL402) considering three paralleled inverters.

The system starts operating with a linear load consisting of at 50% of the rated power. Then, the current GFI is disconnected from the system. Fig. 18 shows the load voltage and output currents for this test. The moment the inverter 1 is disconnected from the circuit, its output current drops to zero. At the same moment, inverter 2 receives a fail flag signal from the CAN bus, and takes place as new GFI. During the transient, the output voltage suffers a small voltage drop due to the loss of power supplied by inverter 1. The voltage amplitude is restored by the new GFI, reaching steady -state after about one period of the grid fundamental frequency.

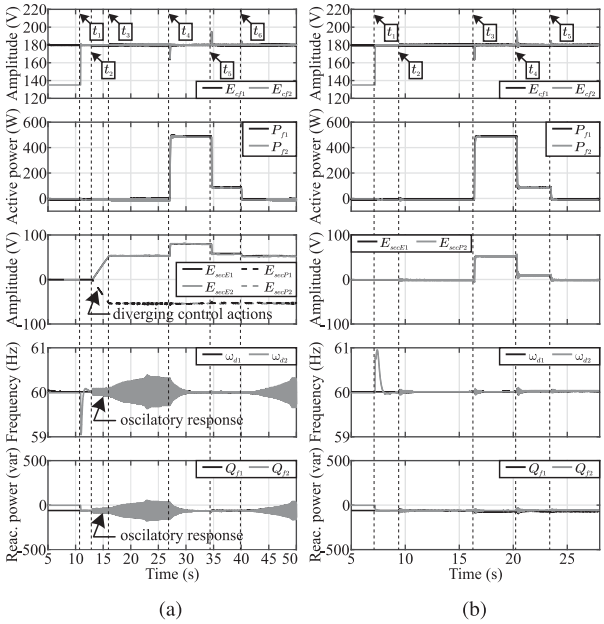

Fig. 19. Comparison of the control systems. (a) Control system proposed in [4] and [5] in its equivalent form for the resistive droop method. (b) Hierarchical control with separation of concerns.

C. Tradeoff Between Voltage Regulation and Power Sharing

In order to demonstrate the inherent conflict between voltage regulation and power sharing, a few tests are carried out. Particularly, the control system from [4], [5] is considered in its equivalent form for the resistive droop control. In this scenario, the secondary control of each inverter operates simultaneously with all secondary control loops.

The tests are carried out considering the normal operating mode. So, for voltage regulation, all inverters operate simultaneously with voltage restoration and active power control loops. Similarly, for frequency regulation, all inverters operate simultaneously with the PLL and with reactive power control loop. The controller gains used are the same previously presented in Table IV.

It is worth noting that the integral signals of the amplitude restoration control loop (I_{eE}) and active power control loop (I_{eP}) are limited to a maximum value of $I_{\text{emax}} = \pm 7$. Fig. 19(a) shows the amplitudes, frequencies, active and reactive powers, and the secondary control signals that act in the amplitude setpoint for the two inverters. Inverter 1 starts operating at no load and at the time indicated by t_1, inverter 2 starts the synchronization process, connecting to the output bus at t_2. The instant the inverters start to operate in parallel, the control signals of the amplitude restoration (E_{secE1}, E_{secE2}) and active

power (E_{secP1}, E_{secP2}) control loops assume opposite directions on both inverters, until the integral signals of the active power control loop reach the saturation value, at t_3. At this moment, the amplitude restoration control loop stabilizes. Significant oscillations can be seen in the frequency and reactive power for both inverters while the system remains at the no load condition. This is due to the interaction between the PLL and reactive power control loops acting simultaneously on all inverters. At time t_4, a linear load step consisting of 100% of the rated power is applied. One can see the operation of the amplitude restoration control loop, whose control signal increases in order to compensate for the voltage drop caused by the droop control and virtual resistance. At t_5 and t_6, resistive load steps equivalent to 80% and 20% of the rated power are removed, respectively. During the application of the load steps, the integral signal of the active power control loop remains at the saturation value, while small corrections can be observed in the control signal due to the action of proportional term. It is worth noting that when no saturation is considered for I_{emax}, the control signals of the amplitude restoration and active power control loops increase in opposite directions indefinitely, characterizing the system as unstable.

Similarly, Fig. 19(b) shows the same test considering the hierarchical control with separations of concerns proposed in the article. The GFI starts operating at no load condition and at t_1, the GSI starts the synchronization process, connecting to the output bus at t_2. At the instant of connection, only small disturbances can be seen in the control signals of the amplitude restoration and active power control loops. In t_3, a linear load step consisting of 100% of the rated power is applied. One can see the operation of the amplitude restoration control loop of the GFI, whose control signal increases in order to compensate the voltage drop caused by the droop control and the virtual resistance. The control signal of the active power loop follows the control signal of the restoration control loop so that the GSI provides the same power as the GFI. At the time instants t_4 and t_5, resistive loads steps equivalent to 80% and 20% of the rated power are removed, respectively. Different from the results seen in Fig. 19(a), the secondary control signals are stable and well defined throughout the whole test. Additionally, the frequencies and reactive powers of the inverters are stable and well regulated.

With respect to Fig. 19(a), the performance observed in terms of amplitude regulation and active power sharing proved to be adequate for the evaluated conditions. This is because the proportional signal of the active power control loop still works even when the integral signal is saturated. However, after reaching the saturation value, the the integral signal remained at that condition indefinitely. This could lead to loss of performance in some scenarios.

VI. Conclusion

The proposed distributed hierarchical control is able to minimize the tradeoff between voltage regulation and power sharing often seen in the parallel operation of inverters by assigning distinct functions to each UPS. A series of experimental results have shown that the voltage amplitude was tightly regulated, while the system accurately shared the load power. The amplitude and power sharing errors remained below 1% and 2%, respectively, for the entire load range.

It was also demonstrated that the system is able to remain operational with good performance even with a communication system outage. Hardware-in-the-loop simulations have shown the good transient response of the system for a failure and redefinition of the GFI.

A comparative analysis was carried out in order to demonstrate the compromise between voltage regulation and power sharing, in addition to the limitations of some of the existing control strategies.

After extensive theoretical analysis and experimental confirmation, we believe that the proposed strategy provides a valuable contribution by mitigating some of the limitations of other distributed control methods, in addition to presenting in detail the modeling and control design for each hierarchical level. The simplified models developed in the article allow the adoption of a simple design procedure for the secondary controllers. However, precisely because of this simplicity, they should serve more as guidelines for the design of the controllers, as they do not accurately model some of the dynamics involved in the system. Thus, it would be of interest to conduct future investigations to optimize the secondary controllers by using more complex models, such as the one presented in the Appendix, together with more advanced design methodologies, such as ants colony optimization, particle swarm optimization, and artificial bee colony algorithm, for example. Other topics of interest for future theoretical and experimental studies include operation with a greater number of inverters, analysis of different events, like failure and change of GFI, and operation with UPSs with different specifications.

Appendix
Small-signal Modeling and Eigenvalues Analysis

Two small-signal models were developed to perform a stability analysis, one for normal operating mode and the other for backup mode. These models are based on steady-state power flow analyses [45], [46] for two paralleled inverters, and are valid at the fundamental frequency. From here on, the subscript i will be used to indicate the ith inverter.

There is a dynamic associated with the power filters used in the droop control, which is modeled by

$$\begin{aligned} \dot{P}_{f\text{i}} &= -\omega_{\text{pbP}} P_{f\text{i}} + \omega_{\text{pbP}} P_{\text{i}} \\ \dot{Q}_{f\text{i}} &= -\omega_{\text{pbQ}} Q_{f\text{i}} + \omega_{\text{pbQ}} Q_{\text{i}} \end{aligned} \tag{25}$$

where P_i and Q_i are auxiliary variables that represent, respectively, the instantaneous active and reactive powers of the ith inverter.

There is also a dynamic associated with the phase angle of the inverter voltages. By using the angular position of inverter 1 as the reference for the system's rotational representation [47], the order of the system can be reduced by one state, as the phase angle of inverter 1 in relation to itself is zero, while for inverter 2 it is given by

$$\dot{\delta}_2 = \omega_{d2} - \omega_{d1}. \tag{26}$$

The secondary controller makes use of the voltage amplitude of each inverter. There is a dynamic associated to the filters used in the calculation of these amplitudes, which is given by

$$\dot{E}_{cfi} = -\omega_{pbE} E_{cfi} + \omega_{pbE} E_{ci} \tag{27}$$

where E_{ci} is an auxiliary variable that represents the instantaneous output voltage amplitude of the ith inverter.

Finally, there are dynamics associated to the integral signal of the secondary controllers. These dynamics are modeled by

$$\begin{aligned} \dot{Ie}_E &= E_{\text{ref}} - \frac{E_{cf1} + E_{cf1}}{2} \\ \dot{Ie}_P &= \frac{(P_{f1} + P_{f2})}{2} - P_{f2} \\ \dot{Ie}_\omega &= \omega_{\text{ref}} - \frac{\omega_{d1} + \omega_{d2}}{2} \\ \dot{Ie}_Q &= \frac{(Q_{f1} + Q_{f2})}{2} - Q_{f2} \end{aligned} \tag{28}$$

where Ie_E, Ie_P, Ie_ω, and Ie_Q are states that represent the integration of the tracking errors of amplitude, frequency, and active and reactive powers over time, respectively.

The auxiliary variables P_i, Q_i, and E_{ci} from (25) and (27) are obtained from the power flow analysis on the circuit shown in Fig. 20, which represents two inverters feeding a load with impedance $Z_L = R_L + jX_L$. The inverters are connected to the load by means of an equivalent output resistance, which is considered equal to the virtual resistance. By performing the power flow analysis, definition of the the auxiliary variables is obtained in (29), where the currents are defined by (30), as shown at the bottom of this page.

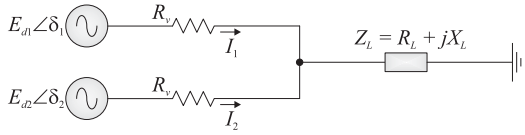

Fig. 20. Representation of 2 parallel-connected inverters.

The amplitudes E_{d1} and E_{d2} in (29) and (30) and the frequencies ω_{d1} and ω_{d2} in (26) are defined by

$$\begin{aligned} E_{d1} &= E_{\text{set1}} - n_d P_{f1}, \quad E_{d2} = E_{\text{set2}} - n_d P_{f2} \\ \omega_{d1} &= \omega_{\text{set1}} + m_d Q_{f1}, \quad \omega_{d2} = \omega_{\text{set2}} + m_d Q_{f2}. \end{aligned} \tag{31}$$

The setpoint for amplitude and frequency are defined by the secondary control, which has different control loops, depending on the UPS operating mode. In this way, two distinct models are obtained, which are presented below.

A. Small-Signal Model for Normal Operating Mode

In normal mode, the GFI operates with a voltage restoration loop, while the frequency setpoint is defined by the PLL, which is not included in the modeling. Thus, the setpoints for amplitude and frequency for the GFI in normal mode are given by (32), where E_{secE} is an auxiliary variable that represents the control signal of the amplitude restoration control loop

$$E_{\text{set1}} = E_{\text{ref}} + E_{\text{secE}}, \quad \omega_{\text{set1}} = \omega_{\text{ref}}. \tag{32}$$

For the GSI, the amplitude setpoint is adjusted by the active power sharing control loop, while the frequency setpoint is adjusted by the reactive power sharing control loop. Thus, the setpoints for amplitude and frequency for the GSI in normal

$$\begin{aligned}
P_1 &= \frac{{E_{d1}}^2\left({R_L}^2 + R_v R_L + {X_L}^2\right) - {E_{d2}}^2\left({R_L}^2 - {X_L}^2\right)}{2{R_v}^3 + 8{R_v}^2 R_L + 8R_v{R_L}^2 + 8R_v{X_L}^2} + \frac{E_{d1}E_{d2}\left(R_v R_L\cos(\delta_2) - R_v X_L \sin(\delta_2)\right)}{2{R_v}^3 + 8{R_v}^2 R_L + 8R_v{R_L}^2 + 8R_v{X_L}^2} \\
Q_1 &= \frac{{E_{d1}}^2 R_v X_L}{2{R_v}^3 + 8{R_v}^2 R_L + 8R_v{R_L}^2 + 8R_v{X_L}^2} + \frac{E_{d1}E_{d2}\left(\left(2{R_L}^2 + R_v R_L + 2{X_L}^2\right)\sin(\delta_2) + R_v X_L\cos(\delta_2)\right)}{2{R_v}^3 + 8{R_v}^2 R_L + 8R_v{R_L}^2 + 8R_v{X_L}^2} \\
P_2 &= \frac{-{E_{d1}}^2\left({R_L}^2 + {X_L}^2\right) + {E_{d2}}^2\left({R_L}^2 + R_v R_L + {X_L}^2\right)}{2{R_v}^3 + 8{R_v}^2 R_L + 8R_v{R_L}^2 + 8R_v{X_L}^2} + \frac{E_{d1}E_{d2}\left(R_v R_L\cos(\delta_2) + R_v X_L \sin(\delta_2)\right)}{2{R_v}^3 + 8{R_v}^2 R_L + 8R_v{R_L}^2 + 8R_v{X_L}^2} \\
Q_2 &= \frac{{E_{d1}}^2 R_v X_L}{2{R_v}^3 + 8{R_v}^2 R_L + 8R_v{R_L}^2 + 8R_v{X_L}^2} + \frac{E_{d1}E_{d2}\left(\left(2{R_L}^2 + R_v R_L + 2{X_L}^2\right)\sin(\delta_2) + R_v X_L\cos(\delta_2)\right)}{2{R_v}^3 + 8{R_v}^2 R_L + 8R_v{R_L}^2 + 8R_v{X_L}^2} \\
E_{ci} &= \sqrt{Re\left(E_{di} - R_v\vec{I}_i\right)^2 + Im\left(E_{di} - R_v\vec{I}_i\right)^2}
\end{aligned} \tag{29}$$

$$\begin{aligned}
\vec{I}_1 &= \frac{E_{d1}\left(2{R_L}^2 + 3R_v R_L + 2{X_L}^2 + {R_v}^2\right)}{4{R_L}^2 R_v + 4R_L{R_v}^2 + {R_v}^3 + 4R_v{X_L}^2} + \frac{E_{d2}\left(R_v X_L\sin(\delta_2) - \cos(\delta_2)\left(2{R_L}^2 + R_v R_L + 2{X_L}^2\right)\right)}{4{R_L}^2 R_v + 4R_L{R_v}^2 + {R_v}^3 + 4R_v{X_L}^2} \\
&\quad + \frac{-jE_{d1}R_v X_L}{4{R_L}^2 R_v + 4R_L{R_v}^2 + {R_v}^3 + 4R_v{X_L}^2} + \frac{jE_{d2}\left(\left(2{R_L}^2 + R_v R_L + 2{X_L}^2\right)\sin(\delta_2) + R_v X_L\cos(\delta_2)\right)}{4{R_L}^2 R_v + 4R_L{R_v}^2 + {R_v}^3 + 4R_v{X_L}^2} \\
\vec{I}_2 &= \frac{-E_{d1}\left(2{R_L}^2 + R_v R_L + 2{X_L}^2\right)}{4{R_L}^2 R_v + 4R_L{R_v}^2 + {R_v}^3 + 4R_v{X_L}^2} + \frac{E_{d2}\left(\left(2{R_L}^2 + 3R_v R_L + 2{X_L}^2 + {R_v}^2\right)\cos(\delta_2) + R_v X_L\sin(\delta_2)\right)}{4{R_L}^2 R_v + 4R_L{R_v}^2 + {R_v}^3 + 4R_v{X_L}^2} \\
&\quad + \frac{j-E_{d1}R_v X_L}{4{R_L}^2 R_v + 4R_L{R_v}^2 + {R_v}^3 + 4R_v{X_L}^2} + \frac{jE_{d2}\left(\left(2{R_L}^2 + 3R_v R_L + 2{X_L}^2 + {R_v}^2\right)\sin(\delta_2) - R_v X_L\cos(\delta_2)\right)}{4{R_L}^2 R_v + 4R_L{R_v}^2 + {R_v}^3 + 4R_v{X_L}^2}
\end{aligned} \tag{30}$$

mode are given by (33), where E_{secP} and ω_{secQ} are auxiliary variables that represent the control signal of active and reactive power sharing control loops, respectively

$$E_{\text{set2}} = E_{\text{ref}} + E_{\text{secP}}, \quad \omega_{\text{set2}} = \omega_{\text{ref}} + \omega_{\text{secQ}}. \tag{33}$$

The auxiliary variables that represents the control signal of the secondary controllers in normal mode (Fig. 5) are

$$\begin{aligned} E_{\text{secE}} &= k_{pE}\left(E_{\text{ref}} - \tfrac{E_{cf1}+E_{cf2}}{2}\right) + k_{iE} Ie_E \\ E_{\text{secP}} &= k_{pP}\left(\tfrac{P_{f1}+P_{f2}}{2} - P_{f2}\right) + k_{iP} Ie_P \\ \omega_{\text{secQ}} &= k_{pQ}\left(\tfrac{Q_{f1}+Q_{f2}}{2} - Q_{f2}\right) + k_{iQ} Ie_Q. \end{aligned} \tag{34}$$

Finally, the dynamic equations for the normal mode are obtained by grouping the states represented in (25)–(28), with the exception of Ie_ω. The resulting dynamic equations are

$$\begin{aligned} \dot{P}_{f1} &= -\omega_{\text{pbP}} P_{f1} + \omega_{\text{pbP}} P_1 \\ \dot{Q}_{f1} &= -\omega_{\text{pbQ}} Q_{f1} + \omega_{\text{pbQ}} Q_1 \\ \dot{E}_{cf1} &= -\omega_{\text{pbE}} E_{cf1} + \omega_{\text{pbE}} E_{c1} \\ \dot{Ie}_E &= E_{\text{ref}} - \frac{E_{cf1} + E_{cf1}}{2} \\ \dot{P}_{f2} &= -\omega_{\text{pbP}} P_{f2} + \omega_{\text{pbP}} P_2 \\ \dot{Q}_{f2} &= -\omega_{\text{pbQ}} Q_{f2} + \omega_{\text{pbQ}} Q_2 \\ \dot{\delta}_2 &= \omega_{d2} - \omega_{d1} \\ \dot{E}_{cf2} &= -\omega_{\text{pbE}} E_{cf2} + \omega_{\text{pbE}} E_{c2} \\ \dot{Ie}_P &= \frac{(P_{f1} + P_{f2})}{2} - P_{f2} \\ \dot{Ie}_Q &= \frac{(Q_{f1} + Q_{f2})}{2} - Q_{f2}. \end{aligned} \tag{35}$$

The auxiliary variables P_1, P_2, Q_1, and Q_2 used in (35) are defined by (29); the currents $\vec{I}_1$ and $\vec{I}_2$ by (30); and the voltage amplitudes and frequencies E_{d1}, E_{d2}, ω_{d1}, and ω_{d2} by (31), respectively. Finally, the amplitude and frequency setpoints used in (31) are defined in (32) and (33).

The equilibrium points of the system can be obtained by solving (35) considering the derivative terms equal to zero. The Jacobian matrix of the system is obtained by linearizing (35) around the equilibrium points.

B. Small-Signal Model for the Backup Mode

For the backup mode, what changes in relation to the normal mode is that the GFI operates with the frequency restoration control loop. In this case, the frequency setpoint of the GFI is given by (36), where $\omega_{\text{sec}\omega}$ is an auxiliary variable that represents the control signal of the frequency restoration control loop, obtained from Fig. 5, and given by (37)

$$\omega_{\text{set1}} = \omega_{\text{ref}} + \omega_{\text{sec}\omega} \tag{36}$$

$$\omega_{\text{sec}\omega} = k_{p\omega}\left(\omega_{\text{ref}} - \frac{\omega_{d1} + \omega_{d2}}{2}\right) + k_{i\omega} Ie_\omega. \tag{37}$$

The dynamic equations for the backup mode can be obtained by grouping the states represented in (25)–(28). The resulting dynamic equations are summarized below

$$\begin{aligned} \dot{P}_{f1} &= -\omega_{\text{pbP}} P_{f1} + \omega_{\text{pbP}} P_1 \\ \dot{Q}_{f1} &= -\omega_{\text{pbQ}} Q_{f1} + \omega_{\text{pbQ}} Q_1 \\ \dot{E}_{cf1} &= -\omega_{\text{pbE}} E_{cf1} + \omega_{\text{pbE}} E_{c1} \\ \dot{Ie}_E &= E_{\text{ref}} - \frac{E_{cf1} + E_{cf1}}{2} \\ \dot{Ie}_\omega &= \omega_{\text{ref}} - \frac{\omega_{d1} + \omega_{d2}}{2} \\ \dot{P}_{f2} &= -\omega_{\text{pbP}} P_{f2} + \omega_{\text{pbP}} P_2 \\ \dot{Q}_{f2} &= -\omega_{\text{pbQ}} Q_{f2} + \omega_{\text{pbQ}} Q_2 \\ \dot{\delta}_2 &= \omega_{d2} - \omega_{d1} \\ \dot{E}_{cf2} &= -\omega_{\text{pbE}} E_{cf2} + \omega_{\text{pbE}} E_{c2} \\ \dot{Ie}_P &= \frac{(P_{f1} + P_{f2})}{2} - P_{f2} \\ \dot{Ie}_Q &= \frac{(Q_{f1} + Q_{f2})}{2} - Q_{f2}. \end{aligned} \tag{38}$$

The auxiliary variables P_1, P_2, Q_1, and Q_2 used in (38) are defined by (29); the currents $\vec{I}_1$ and $\vec{I}_2$ by (30); and the voltage amplitudes and frequencies E_{d1}, E_{d2}, ω_{d1}, and ω_{d2} by (31), respectively. In the backup mode, the amplitude and frequency setpoints used in (31) are defined by (36) and (33).

Once again, the equilibrium points of the system can be obtained by solving (38) considering the derivative terms equal to zero. The Jacobian matrix of the system is obtained by linearizing (38) around the equilibrium points.

C. Stability Analysis for Load Variations

Below, a stability analysis based on the eigenvalues of the system for normal and backup modes is presented. A first analysis considering a variation in the load resistance for an active power range of 0.1% up to the nominal value is carried out. In this analysis, the reactive power of the load is zero, so $X_L = 0$. Intervals of 10% of active power are used, and for each iteration, the equilibrium points, the Jacobian matrix and the corresponding eigenvalues are calculated. A second condition is considered, where a fixed load resistance equivalent to an active power of $P = 707.1$ W is used, and the load reactance is varied in order to consume a reactive power of $Q = 0$ var up to $Q_{\text{max}} = 707.1$ var (totaling 1 kVA). Reactive power intervals equivalent to 10% of Q_{max} are used and, for each iteration, the equilibrium points, the Jacobian matrix, and the corresponding eigenvalues are calculated.

Fig. 21 shows the closed-loop eigenvalues for varying R_L and X_L in both operating modes. For both the normal and backup operating modes, the system eigenvalues underwent only small variations due to changes in load resistance and reactance, indicating the good robustness of the system.

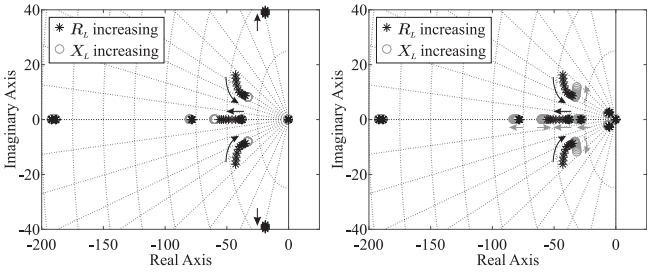

Fig. 21. Closed-loop eigenvalues of the system for variations in load resistance and reactance.

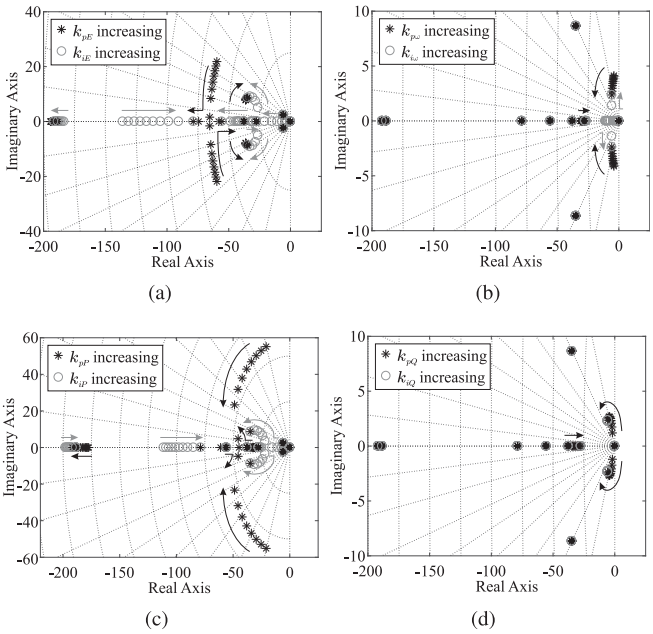

Fig. 22. Closed-loop eigenvalues of the system for variations in the secondary controller gains.

D. Impact of the Secondary Control Parameters

Fig. 22 shows the trajectory of the eigenvalues as a function of the secondary control parameters for each control loop. The PI gains are varied in an interval of 0.1 up to 10 times in relation to gain values presented in Table IV.

As the proportional terms of PI controllers are increased, some of the eigenvalues of the system move toward the unstable region, making the system more oscillatory and eventually leading to instability. The integral term parameter has less significant effects on the dynamics of the system. Similar analysis can be performed for the different parameters of the developed model.

REFERENCES

[1] J. M. Guerrero, L. Hang, and J. Uceda, "Control of distributed uninterruptible power supply systems," *IEEE Trans. Ind. Electron.*, vol. 55, no. 8, pp. 2845–2859, Aug. 2008.

[2] J. M. Guerrero, J. Matas, L. G. Vicuna, and M. Castilla, "Hierarchical control of droop-controlled AC and DC microgrids – A general approach towards standardization," *IEEE Trans. Ind. Electron.*, vol. 58, no. 1, pp. 158–172, Jan. 2011.

[3] J. W. Simpson-Porco, Q. Shafiee, F. Dorfler, J. C. Vásquez, J. M. Guerrero, and F. Bullo, "Secondary frequency and voltage control of islanded microgrids via distributed averaging," *IEEE Trans. Ind. Electron.*, vol. 62, no. 11, pp. 7025–7038, Nov. 2015.

[4] Q. Shafiee, J. M. Guerrero, and J. C. Vásquez, "Distributed secondary control for islanded microgrids–A novel approach," *IEEE Trans. Power Electron.*, vol. 29, no. 2, pp. 1018–1031, Feb. 2014.

[5] Q. Shafiee, C. Stefanovic, T. Dragicevic, P. Popovski, J. C. Vásquez, and J. M. Guerrero, "Robust networked control scheme for distributed secondary control of islanded microgrids," *IEEE Trans. Ind. Electron.*, vol. 61, no. 10, pp. 5363–5374, Oct. 2014.

[6] R. Han, L. Meng, G. Ferrari-Trecate, E. A. A. Coelho, J. C. Vásquez, and J. M. Guerrero, "Containment and consensus-based distributed coordination control to achieve bounded voltage and precise reactive power sharing in islanded AC microgrids," *IEEE Trans. Ind. Appl.*, vol. 53, no. 6, pp. 5187–5199, Nov. 2017.

[7] Y. Khayat *et al.*, "On the secondary control architectures of AC microgrids: An overview," *IEEE Trans. Power Electron.*, vol. 35, no. 6, pp. 6482–6500, Jun. 2020.

[8] X. Yang, Y. Du, J. Su, L. Chang, Y. Shi, and J. Lai, "An optimal secondary voltage control strategy for an islanded multibus microgrid," *IEEE Trans. Emerg. Sel. Topics Power Electron.*, vol. 4, no. 4, pp. 1236–1246, Dec. 2016.

[9] Y. Guan, J. C. Vasquez, and J. M. Guerrero, "Coordinated secondary control for balanced discharge rate of energy storage system in islanded AC microgrids," *IEEE Trans. Ind. Appl.*, vol. 52, no. 6, pp. 5019–5028, Nov./Dec. 2016.

[10] Y. Han, P. Shen, X. Zhao, and J. M. Guerrero, "An enhanced power sharing scheme for voltage unbalance and harmonics compensation in an islanded AC microgrid," *IEEE Trans. Energy Convers.*, vol. 31, no. 3, pp. 1037–1050, Sep. 2016.

[11] M. H. Andishgar, E. Gholipour, and R.-A. Hooshmand, "Voltage quality enhancement in islanded microgrids with multi-voltage quality requirements at different buses," *IET Gener., Transmiss. Distrib.*, vol. 12, no. 9, pp. 2173–2180, 2018.

[12] T. Dragicevic, R. Heydari, and F. Blaabjerg, "Super-high bandwidth secondary control of AC microgrids," in *Proc. IEEE Appl. Power Electron. Conf. Expo.*, 2018, pp. 3036–3042.

[13] M. Jafari *et al.*, "Adaptive neural network based intelligent secondary control for microgrids," in *Proc. IEEE Texas Power Energy Conf.*, 2018, pp. 1–6.

[14] S. Acharya, M. S. El-Moursi, A. Al-Hinai, A. S. Al-Sumaiti, and H. H. Zeineldin, "A control strategy for voltage unbalance mitigation in an islanded microgrid considering demand side management capability," *IEEE Trans. Smart Grid*, vol. 10, no. 3, pp. 2558–2568, May 2019.

[15] Q. C. Zhong, "Robust droop controller for accurate proportional load sharing among inverters operated in parallel," *IEEE Trans. Ind. Electron.*, vol. 60, no. 4, pp. 1281–1290, Apr. 2013.

[16] Q. C. Zhong and Y. Zeng, "Universal droop control of inverters with different types of output impedance," *IEEE Access*, vol. 4, pp. 702–712, Feb. 2016.

[17] N. Xia, H. B. Gooi, S. Chen, and W. Hu, "Decentralized state estimation for hybrid AC/DC microgrids," *IEEE Syst. J.*, vol. 12, no. 1, pp. 434–443, Mar. 2018.

[18] Y. Khayat *et al.*, "Communication-less optimal frequency control of islanded microgrids," in *Proc. 20th Eur. Conf. Power Electron. Appl.*, 2018, pp. 1–8.

[19] Z. Zhang, C. Dou, D. Yue, B. Zhang, and W. Luo, "A decentralized control method for frequency restoration and accurate reactive power sharing in islanded microgrids," *J. Franklin Inst.*, vol. 355, no. 17, pp. 8874–8890, 2018.

[20] Y. Han, H. Li, L. Xu, X. Zhao, and J. M. Guerrero, "Analysis of washout filter-based power sharing strategy—An equivalent secondary controller for islanded microgrid without LBC lines," *IEEE Trans. Smart Grid*, vol. 9, no. 5, pp. 4061–4076, Sep. 2018.

[21] E. Weitenberg, Y. Jiang, C. Zhao, E. Mallada, C. De Persis, and F. DÃrfler, "Robust decentralized secondary frequency control in power systems: Merits and tradeoffs," *IEEE Trans. Autom. Control*, vol. 64, no. 10, pp. 3967–3982, Oct. 2019.

[22] Y. Khayat *et al.*, "Decentralized optimal frequency control in autonomous microgrids," *IEEE Trans. Power Syst.*, vol. 34, no. 3, pp. 2345–2353, May 2019.

[23] M. Castilla, A. Camacho, J. Miret, M. Velasco, and P. MartÃ, "Local secondary control for inverter-based islanded microgrids with accurate active power sharing under high-load conditions," *IEEE Trans. Ind. Electron.*, vol. 66, no. 4, pp. 2529–2539, Apr. 2019.

[24] M. S. Golsorkhi, Q. Shafiee, D. D.-C. Lu, and J. M. Guerrero, "Distributed control of low-voltage resistive AC microgrids," *IEEE Trans. Energy Convers.*, vol. 34, no. 2, pp. 573–584, Jun. 2019.
[25] F. Dorfler, J. W. Simpson-Porco, and F. Bullo, "Breaking the hierarchy: Distributed control and economic optimality in microgrids," *IEEE Control Netw. Syst.*, vol. 3, no. 3, pp. 241–253, Sep. 2016.
[26] M. S. Golsorkhi, D. Lu, Q. Shafiee, and J. M. Guerrero, "Distributed voltage control and load sharing for inverter-interfaced microgrid with resistive lines," in *Proc. Energy Convers. Congr. Expo.*, 2016, pp. 1–7.
[27] V. Nasirian, Q. Shafiee, J. M. Guerrero, F. L. Lewis, and A. Davoudi, "Droop-free distributed control for AC microgrids," *IEEE Trans. Power Electron.*, vol. 31, no. 2, pp. 1600–1617, Feb. 2016.
[28] B. Wei, Y. Gui, S. Trujillo, J. M. Guerrero, J. C. Vásquez, and A. Marzábal, "Distributed average integral secondary control for modular ups systems-based microgrids," *IEEE Trans. Power Electron.*, vol. 34, no. 7, pp. 6922–6936, Jul. 2019.
[29] Z. Wang, J. He, Y. Xu, and F. Zhang, "Distributed control of VSC-MTDC systems considering tradeoff between voltage regulation and power sharing," *IEEE Trans. Power Syst.*, vol. 35, no. 3, pp. 1812–1821, May 2020.
[30] R. Han, L. Meng, J. M. Guerrero, Q. Sun, and J. C. Vásquez, "Coupling/tradeoff analysis and novel containment control for reactive power, output voltage in islanded micro-grid," in *Proc. 42nd Annu. Conf. IEEE Ind. Electron. Soc.*, 2016, pp. 5205–5210.
[31] J. Llanos, D. E. Olivares, J. W. Simpson-Porco, M. Kazerani, and D. Sáez, "A novel distributed control strategy for optimal dispatch of isolated microgrids considering congestion," *IEEE Trans. Smart Grid*, vol. 10, no. 6, pp. 6595–6606, Nov. 2019.
[32] Q. Shafiee, V. Nasirian, J. C. Vásquez, J. M. Guerrero, and A. Davoudi, "A multi-functional fully distributed control framework for AC microgrids," *IEEE Trans. Smart Grid*, vol. 9, no. 4, pp. 3247–3258, Jul. 2018.
[33] D. De and V. Ramanarayanan, "Decentralized parallel operation of inverters sharing unbalanced and nonlinear loads," *IEEE Trans. Power Electron.*, vol. 25, no. 12, pp. 3015–3025, Dec. 2010.
[34] A. Tuladhar, H. Jin, T. Unger, and K. Mauch, "Parallel operation of single phase inverter modules with no control interconnections," in *Proc. Appl. Power Electron. Conf.*, 1997, pp. 94–100.
[35] J. M. Guerrero, J. Matas, L. Garcia de Vicuna, M. Castilla, and J. Miret, "Decentralized control for parallel operation of distributed generation inverters using resistive output impedance," *IEEE Trans. Ind. Electron.*, vol. 54, no. 2, pp. 994–1004, Apr. 2007.
[36] W. Yao, M. Chen, J. Matas, J. M. Guerrero, and Z.-H. Qian, "Design and analysis of the droop control method for parallel inverters considering the impact of the complex impedance on the power sharing," *IEEE Trans. Ind. Electron.*, vol. 58, no. 2, pp. 576–588, Feb. 2011.
[37] S. Golestan, J. M. Guerrero, and J. C. Vásquez, "Three-phase PLLs: A review of recent advances," *IEEE Trans. Power Electron.*, vol. 32, no. 3, pp. 1894–1907, Mar. 2017.
[38] M. Ciobotaru, R. Teodorescu, and F. Blaabjerg, "A new single-phase PLL structure based on second order generalized integrator," in *Proc. Power Electron. Specialists Conf.*, 2006, pp. 1–6.
[39] M. E. Elkhatib, W. Du, and R. H. Lasseter, "Evaluation of inverter-based grid frequency support using frequency-watt and grid-forming PV inverters," in *Proc. IEEE Power Energy Soc. General Meeting*, 2018, pp. 1–5.
[40] C. A. Albugeri, N. C. D. Pont, T. K. Jappe, S. A. Mussa, and T. B. Lazzarin, "Control system for multi-inverter parallel operation in uninterruptible power systems," *Revista Eletrônica de Potência*, vol. 24, no. 1, pp. 37–46, Mar. 2019.
[41] G. F. Franklin, J. D. Powell, and M. L. Workman, *Digital Control of Dynamic Systems3rd ed*. Boston, MA, USA: Addison-Wesley, 1998.
[42] Y. Han, P. Shen, X. Zhao, and J. M. Guerrero, "Control strategies for islanded microgrid using enhanced hierarchical control structure with multiple current-loop damping schemes," *IEEE Trans. Smart Grid*, vol. 8, no. 3, pp. 1139–1153, May. 2017.
[43] X. Lu, J. M. Guerrero, K. Sun, J. C. Vásquez, R. Teodorescu, and L. Huang, "Hierarchical control of parallel AC–DC converter interfaces for hybrid microgrids," *IEEE Trans. Smart Grid*, vol. 5, no. 2, pp. 683–692, Mar. 2014.
[44] *Uninterruptible Power Systems (UPS) - Part 3: Method of Specifying the Performance and Test Requirements*, IEC Standard 62040–3:2011, 2011.
[45] T. V. Cutsem and C. Vournas, *Voltage Stability of Electric Power Systems*, *2nd ed*. Boston, MA, USA: Kluwer Academic Publishers, 1998.
[46] P. Kundur, *Power System Stability and Control*. *1st ed*. New York, NY, USA: McGraw-Hill, 1994.
[47] P. Sauer and M. Pai, "Power system steady-state stability and the load-flow Jacobian," *IEEE Trans. Power Syst.*, vol. 5, no. 4, pp. 1374–1383, Nov. 1990.